

Supporting information for the paper “Periodic and nonperiodic chiral self- assembled networks from 1,3,5- benzenetricarboxylic acid on Ag(111)”

Josh Lipton-Duffin, Maryam Abyazisani and Jennifer MacLeod
School of Chemistry, Physics and Mechanical Engineering (CPME) and Institute for Future
Environments (IFE), Queensland University of Technology (QUT), Brisbane, Australia

Contents

STM images from TMA on Ag(111) at room temperature, and after moderate annealing.....	2
Evolution of O 1s core level during annealing	4
Gas phase DFT model of hydrogen-bonding between discrete pinwheels.....	6
Epitaxy matrix for knitted pinwheel phase.....	7
Details of chirality in the knitted pinwheel phase	8
Evolution of oxygen and carbon content of the sample	9
Calibration information for the XPS system	10
References	11

STM images from TMA on Ag(111) at room temperature, and after moderate annealing

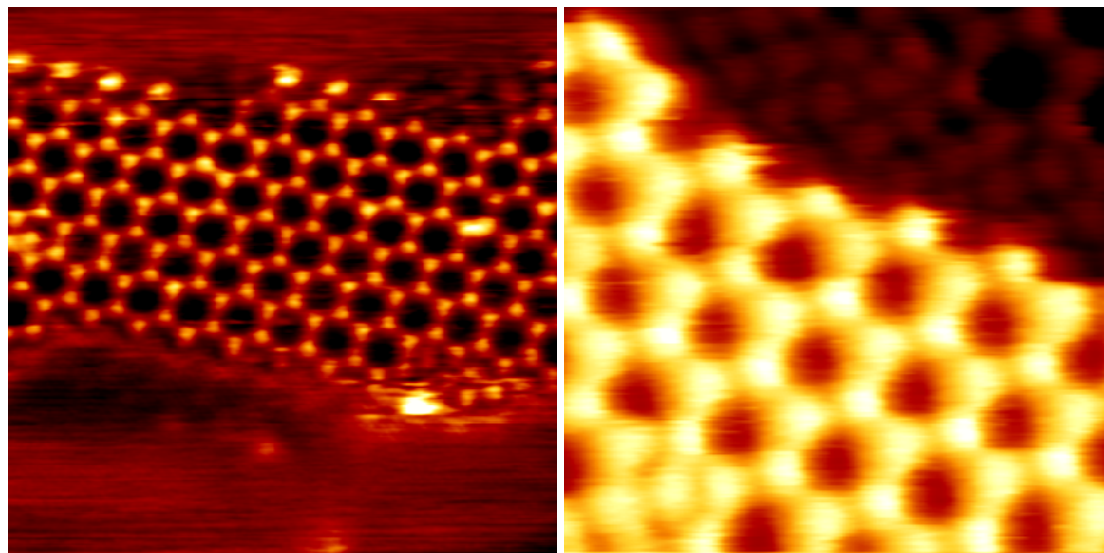


Figure S 1: Submonolayer TMA on Ag(111) deposited at room temperature. Image 1: $(19.2 \text{ nm})^2$, $i_T = 10 \text{ pA}$, $v_B = -1.21 \text{ V}$. Image 2: $(9.1 \text{ nm})^2$, $i_T = 50 \text{ pA}$, $v_B = -1.21 \text{ V}$.

Deposition of TMA on Ag(111) at room temperature leads to the formation of the well-known chicken wire structure, comprising hydrogen dimer bonds between every carboxylic acid group, as has been observed by other groups on this surface in the past.¹ The corresponding XPS (see manuscript Figure 1a and Figure S 2 below) is consistent with the interpretation that 100% of the carboxylic acid groups are intact, and that the arrangement of the molecules is consistent with the phases observed on Au(111) and highly oriented pyrolytic graphite.²⁻⁵

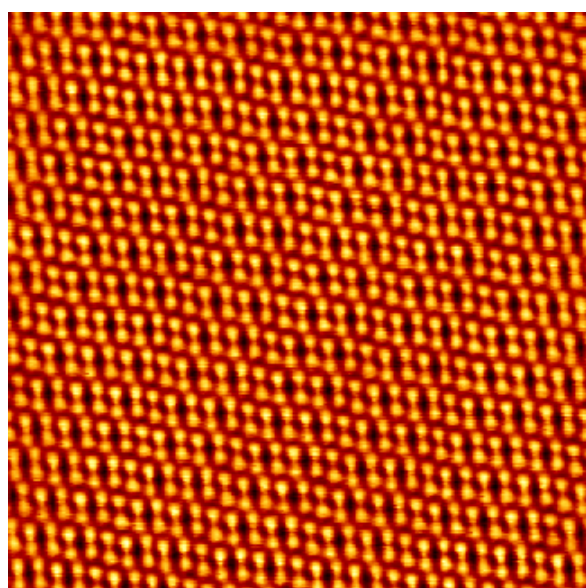


Figure S 2: Dimer phase produced by annealing a TMA/Ag(111) monolayer at 160°C for 5 minutes. $(28.2 \text{ nm})^2$, $i_T = 50 \text{ pA}$, $v_B = -850 \text{ mV}$.

After annealing to 160°C for five minutes, new phase dominates over the surface, consisting of rows of TMA dimers. These have been previously discussed by Payer et al., and are thought to consist of a combination of hydrogen bonding in the intact carboxylic group and ionic hydrogen bonds mediated through the substrate metal atoms.⁶ The XPS measurements for this structure (Figure 1b in the manuscript and Figure S 3 below) suggest a deprotonation level of approximately 33%, or one carboxylic group per molecule, entirely consistent with previous interpretations.

Evolution of O 1s core level during annealing

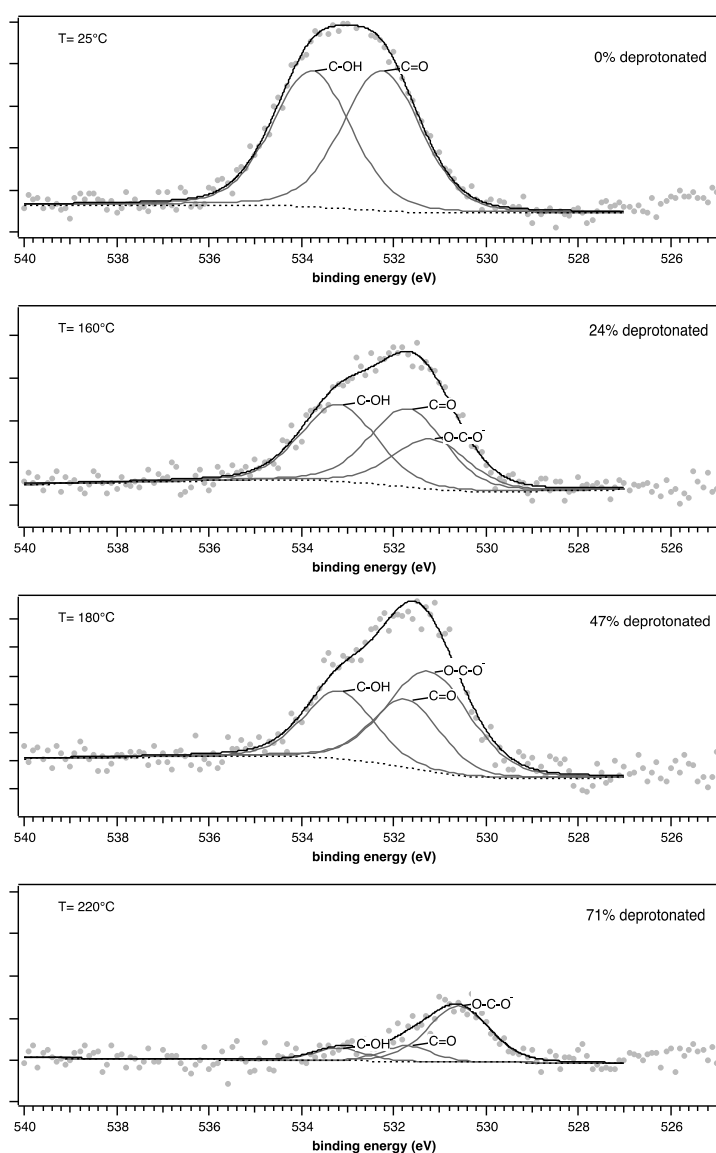


Figure S3: Evolution of O 1s core level during annealing of TMA on Ag(111)

As the surface is annealed, changes in the O 1s core level can also be readily observed, as presented above. For the room temperature surface the lineshape is well-modelled by a pair of peaks with identical intensity, corresponding to the hydroxyl and carbonyl oxygens respectively. As the surface is annealed, a new peak at a lower binding energy emerges, corresponding to the oxygens in the carboxylate group. The intensity ratio of the carboxylate to carboxylic acid peak tracks the ratios extracted from the carbon 1s data (manuscript figure 1) in a consistent manner.

Going from partial deprotonation (24%) to near-full deprotonation (71%) shifts the position of the carboxylate peak from 531.3 eV to 530.5 eV. This is the expected direction for a binding energy shift associated with introducing metal coordination to a previously uncoordinated carboxylate.⁷ We note that this shift direction is somewhat contentious, and that a shift to increased binding energy has been observed for Fe-coordinated carboxylate, which the authors rationalize based on the presumed chemical state of the carboxylate prior to the metal coordination.⁷

The observed shift to lower binding energy of the carboxylate peak does not onset until very high deprotonation levels (74%), whereas the STM-observed surface structures comprise metal coordinated hexamers starting from deprotonation levels around 50%. The reason for the suppression of the binding energy shift at moderate deprotonation levels is not immediately clear, but could imply, for example, that the nature of the metal coordination changes as the knitted pinwheel structure begins to dominate. This interpretation is not obviously indicated or supported by our STM data, but would account for the change observed in O1s.

Gas phase DFT model of hydrogen-bonding between discrete pinwheels

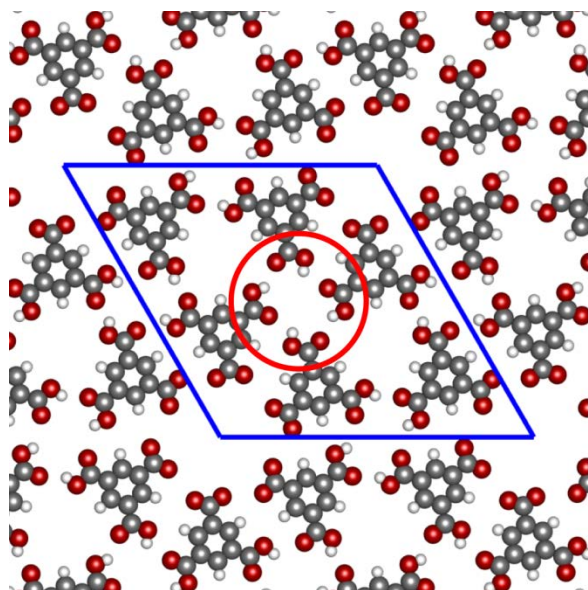


Figure S 4: Gas phase model of the pinwheel phase. The unit cell (shown in blue) contains six individual molecules. There are three cyclic tetramer hydrogen bonds in the cell, one of which is circled in red.

A gas phase assembly of the pinwheel structure was modelled in Gaussian 09⁸ using the B3LYP functional with a 6-31G(d,p) basis set, which was chosen for consistency with our previous calculations. The model consists of six individual TMA-like atoms, each with a single deprotonated carboxyl group. However, as the metal coordination at the center of the pores is difficult to account for without knowing the nature of the cluster, the carboxylate moieties were replaced with a single hydrogen for the optimisation, effectively meaning that the assembly consists of isophthalic acid rather than TMA. This permits us to focus on the stabilisation energy of the cyclic hydrogen-bonded tetramer that appears at the edges of each pinwheel. The cell contains a total of three tetramers (12 individual bonding groups).

The geometry of the cell after optimisation is hexagonal, with a lattice constant of approximately 2.39 Å, which is slightly larger than the epitaxially observed unit cell of 2.31 Å. The total stabilisation energy per unit cell is -6.6 kcal/mol, which is -2.2 kcal/mol per tetramer, or -0.55 kcal/mol per molecule. This energy is essentially equal to the thermal energy $k_B T$ at room temperature, but overall the cohesive energy of the tetramer is likely to be a cooperative effect in producing the structure.

Epitaxy matrix for knitted pinwheel phase

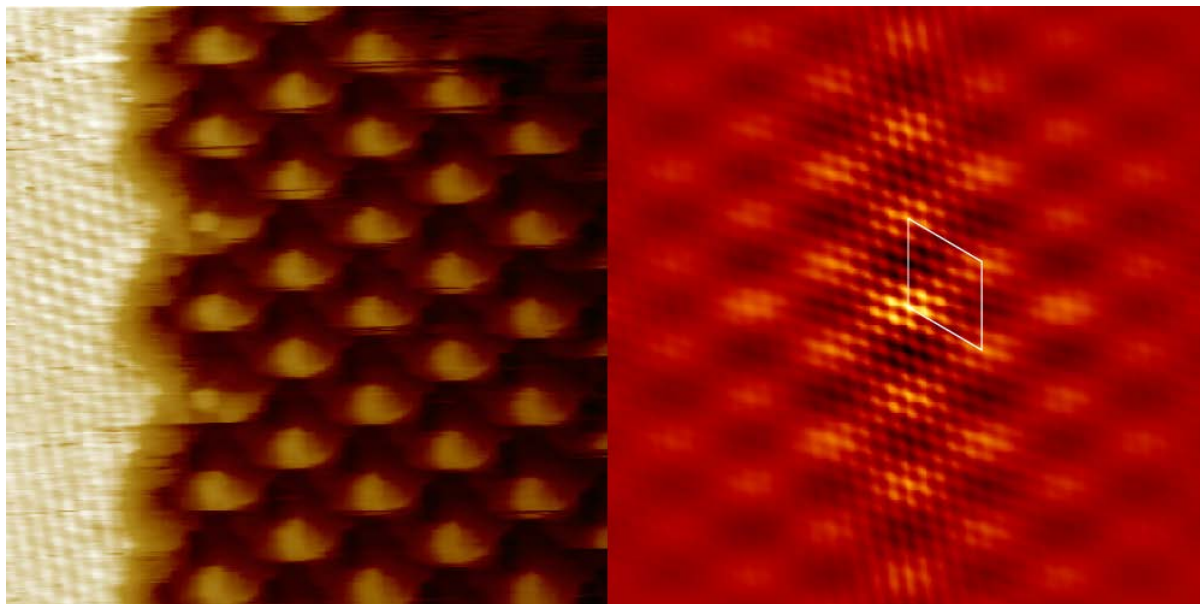


Figure S 5: Image containing atomic resolution of the substrate with the knitted pinwheel phase, and its autocorrelation. $(8.7 \text{ nm})^2$, $i_T = 30 \text{ pA}$, $v_B = -800 \text{ mV}$.

Images where the substrate atoms can be simultaneously resolved with the knitted pinwheel structure permit the extraction of the epitaxy matrix for the phase. Even though the molecular contrast is poor, the periodicity of the phase is still clearly visible in the image *via* the bright adatom feature at the centre of the hexamer. A self-correlation of this image elucidates the epitaxy matrix, which is described by the coincident points of the substrate symmetry points with those of the overlayer phase. The unit cell, drawn in white, describes an overlayer matrix of $\begin{pmatrix} 4 & -1 \\ 1 & 5 \end{pmatrix}$, or $\sqrt{21} \times \sqrt{21} R 56^\circ$.

Details of chirality in the knitted pinwheel phase

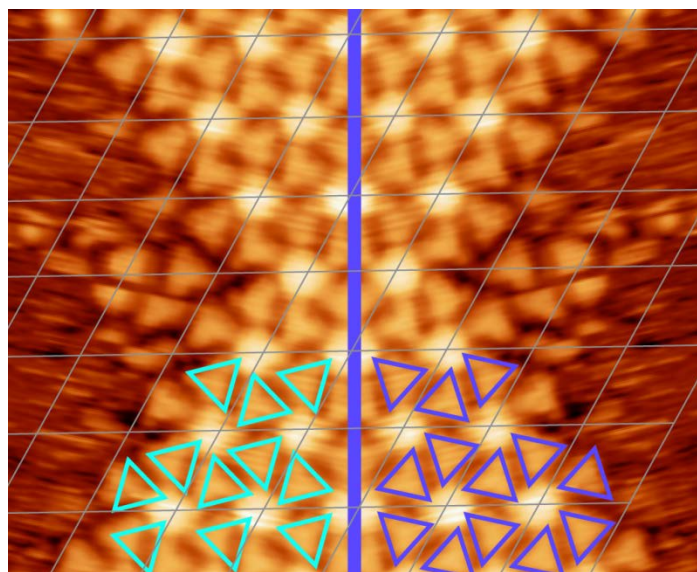


Figure S 6: STM image demonstrating chirality of knitted pinwheel domain

The chirality of the knitted pinwheel structure is readily verified by inspection of Figure S 6. An STM image of a knitted pinwheel domain is reflected along a high-symmetry line of the lattice, and the reflected copy is oriented next to the original image. The grey overlaid lines clearly indicate the registry of the reflection with the original image.

Individual molecules are imaged with a triangular shape, with a slight Y-shaped profile. The orientation of the two molecules per unit cell is shown with cyan triangles in the reflected copy (left) and blue triangles in the original image (right). The molecules are rotated by approximately $\pm 15^\circ$ with respect to the unit cell high-symmetry axes.

It is clear that there is no way to map the reflected domain back into registry with the original image via any combination of translations or rotations, and thus the domain is by definition chiral.

Evolution of oxygen and carbon content of the sample

As the surface is annealed a substantial number of molecules desorb from the sample, corresponding to an overall reduction of the signal intensity. To investigate this effect we performed a calculation of the ratio of oxygen to carbon remaining on the surface at each step of the annealing. This analysis was done in two ways, first by comparing the overall intensity of the O 1s core level to the C 1s core level (a.k.a. analysis by region), as well as the intensity of the oxygen-bound carbon signal to the phenyl carbon signal (a.k.a. analysis by subcomponent). This latter method is appealing because it does not require *a priori* knowledge of the analyser transmission function or of relative sensitivity factors pertinent to each element.

Sample	Total counts (phenyl ring)	Total counts (oxygen-bound carbon)	Ratio C-C to C-O
Chickenwire	2376±115	1049±108	2.17±0.13
Dimer	1898±134	1253±391	2.48±0.18
Granular pinwheels	1533±148	809±307	2.1±0.2
Knitted pinwheels	820±106	428±244	3.4±0.9

Table S 1: Analysis by C1s subcomponent to determine the oxygen to carbon ratio

Sample	Total counts (C1s)	Total counts (O1s)	Ratio carbon to oxygen (RSF corrected)
Chickenwire	3351±160	3267±105	1.54±0.09
Dimer	2810±159	2403±106	1.75±0.13
Granular pinwheels	2001±168	2066±117	1.45±0.15
Knitted pinwheels	913±129	577±131	2.4±0.6

Table S 2: Analysis by region to determine the oxygen to carbon ratio

The results are presented in Table S 1 and Table S 2. The error bars are generated by Monte Carlo simulation of the fitting region/components as implemented in the CasaXPS software. Because the transmission function of this instrument is not fully characterised we use a sensitivity factor of $\frac{RSF(O)}{RSF(C)} = 1.5$ for oxygen based on our empirical understanding of the machine.

We note that in the region analysis the oxygen to carbon ratio appears higher than expected after the final annealing step. We may ascribe this to molecules that have reacted at sites like defects and step edges, since the dominant ordered phase, knitted pinwheel, does not comprise decarboxylated molecules. The uncertainty margin is very large for the knitted pinwheel structure, due to the substantial desorption and consequent low signal-to-noise for these spectra. We can therefore only interpret this as weak evidence for decarboxylative events concurrent with the formation of the knitted pinwheel phase.

Calibration information for the XPS system

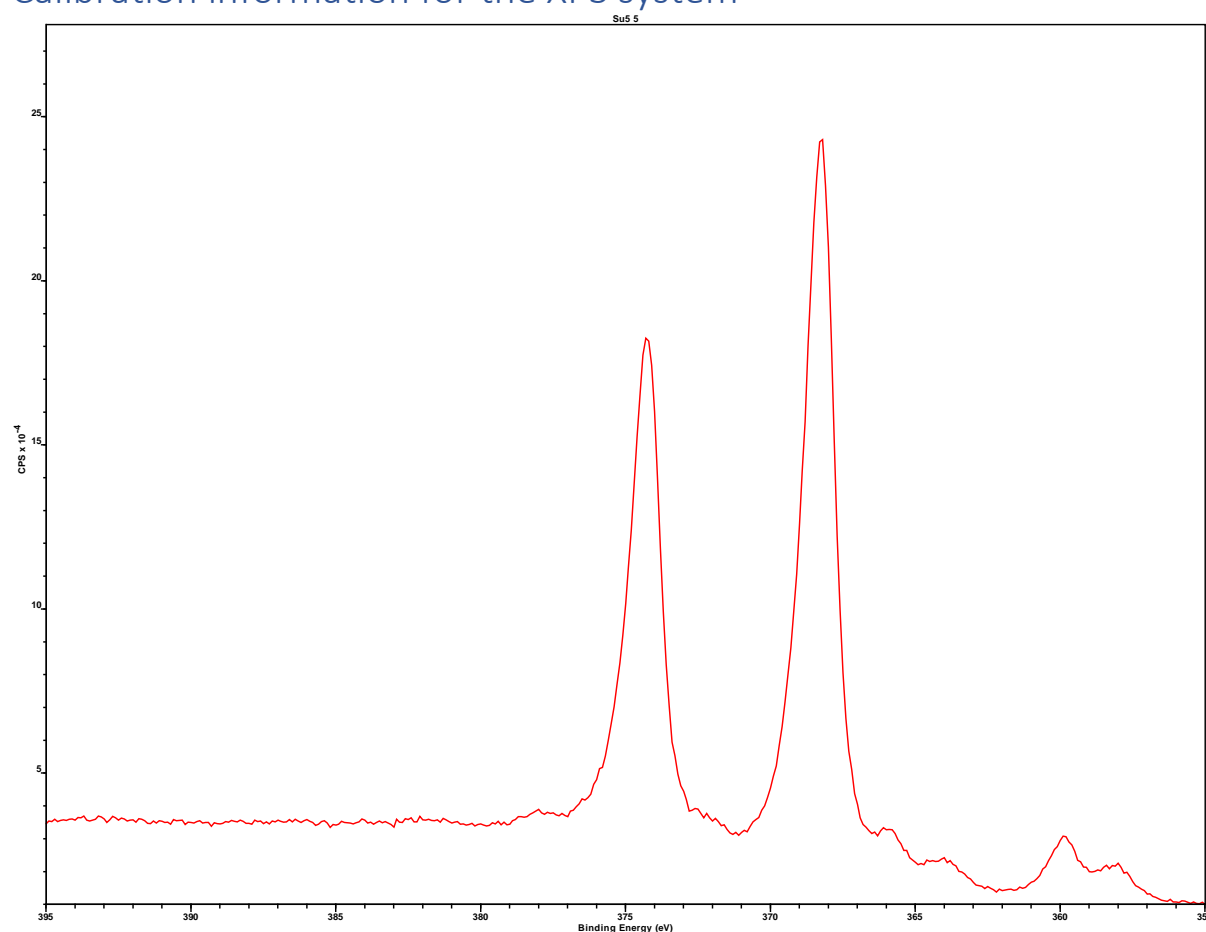


Figure S 7: High resolution XPS scan of the Ag 3d core level

Figure S 7 shows a high resolution scan of the Ag 3d core level. The spectrum exhibits a classic asymmetric shape expected for a metallic element, with characteristic plasmon resonances on the high binding energy side of the doublet, and $K\alpha_{3,4}$ satellites from the achromatic Mg x-ray anode on the low binding energy side.

The $3d_{5/2}$ peak can be fit with an asymmetric lineshape with a peak at a binding energy of 368.2 eV. This matches well with accepted values for this core level, and confirms that the energy scale of our XPS system is properly calibrated.

References

1. N. Lin, D. Payer, A. Dmitriev, T. Strunskus, C. Wöll, J. V. Barth and K. Kern, *Angewandte Chemie International Edition*, 2005, **44**, 1488-1491.
2. S. Griessl, M. Lackinger, M. Edelwirth, M. Hietschold and W. M. Heckl, *Single Molecules*, 2002, **3**, 25-31.
3. J. MacLeod, J. Lipton-Duffin, D. Cui, S. De Feyter and F. Rosei, *Langmuir*, 2015, **31**, 7016-7024.
4. V. Iancu, K.-F. Braun, K. Schouteden and C. Van Haesendonck, *Langmuir*, 2013, **29**, 11593-11599.
5. Y. Ye, W. Sun, Y. Wang, X. Shao, X. Xu, F. Cheng, J. Li and K. Wu, *The Journal of Physical Chemistry C*, 2007, **111**, 10138-10141.
6. D. Payer, A. Comisso, A. Dmitriev, T. Strunskus, N. Lin, C. Wöll, A. DeVita, J. V. Barth and K. Kern, *Chemistry-A European Journal*, 2007, **13**, 3900-3906.
7. S. L. Tait, Y. Wang, G. Costantini, N. Lin, A. Baraldi, F. Esch, L. Petaccia, S. Lizzit and K. Kern, *Journal of the American Chemical Society*, 2008, **130**, 2108-2113.
8. M. J. Frisch, G. W. Trucks, H. B. Schlegel, G. E. Scuseria, M. A. Robb, J. R. Cheeseman, G. Scalmani, V. Barone, B. Mennucci, G. A. Petersson, H. Nakatsuji, M. Caricato, X. Li, H. P. Hratchian, A. F. Izmaylov, J. Bloino, G. Zheng, J. L. Sonnenberg, M. Hada, M. Ehara, K. Toyota, R. Fukuda, J. Hasegawa, M. Ishida, T. Nakajima, Y. Honda, O. Kitao, H. Nakai, T. Vreven, J. J. A. Montgomery, J. E. Peralta, F. Ogliaro, M. Bearpark, J. J. Heyd, E. Brothers, K. N. Kudin, V. N. Staroverov, T. Keith, R. Kobayashi, J. Normand, K. Raghavachari, A. Rendell, J. C. Burant, S. S. Iyengar, J. Tomasi, M. Cossi, N. Rega, J. M. Millam, M. Klene, J. E. Knox, J. B. Cross, V. Bakken, C. Adamo, J. Jaramillo, R. Gomperts, R. E. Stratmann, O. Yazyev, A. J. Austin, R. Cammi, C. Pomelli, J. W. Ochterski, R. L. Martin, K. Morokuma, V. G. Zakrzewski, G. A. Voth, P. Salvador, J. J. Dannenberg, S. Dapprich, A. D. Daniels, O. Farkas, J. B. Foresman, J. V. Ortiz, J. Cioslowski and D. J. Fox, *Journal*, 2010.